

Space charge in liquid argon time-projection chambers: a review of analytical and numerical models, and mitigation methods

Sandro Palestini and Filippo Resnati
CERN, 1211 Geneva 23, Switzerland

Abstract

The subject of space charge in ionisation detectors is reviewed, with particular attention to the case of liquid argon time projection chambers. Analytical and numerical description of the effects on the reconstructed coordinates along the drift and the transverse directions are presented. The cases of limited electron lifetime, of dual-phase detectors with ion feedback, and of detectors with small and comparable ratio between drift length and width are considered. Two design solutions that mitigates the effects are discussed.

1 Introduction

Ionisation detectors, based on gaseous or liquid media, are designed to collect the signal induced by the motion of electrons between polarisation electrodes. In comparison, the signal induced by ions is very low, because their drift velocity is lower by several orders of magnitude. However the low velocity also implies that the ions remain longer in the drift volume: in case of long drift distance or large irradiation, and in particular for liquid detectors, the charge density due to ions may be large enough to affect the electric field that drives the motion of the electrons.¹

Effects of space charge have been studied in calorimeters using liquid krypton [1] and liquid argon [2, 3]. More recently, the relevance and the scope of this subject has widened with the development of large liquid argon imaging devices [7, 8, 9, 10], where the drift volume may be long enough to become sensitive to the space charge due just to the exposure to cosmic rays at the surface of the Earth.

The purpose of this paper is to review the basic formalism describing space-charge effects in ionisation detectors. First, the simplest one-dimensional treatment will be reviewed, followed by a discussions of the effects of charge-yield dependence on the electric field, and of electron attachment, with the related presence of negative ions. Multi-dimensional cases are discussed in terms of boundary conditions on the side walls, and of aspect ratio (depth vs. width) of the drift volume. The case of dual-phase detector with injection of positive ions at the anode end of the drift volume is discussed. Two mitigation methods are considered, dealing respectively with the effects on the drift coordinate and on the transverse coordinates. Throughout the work, scaling laws are discussed, aiming at relations that could be used as guidelines for detectors operated in different conditions and with different geometry. Comparison between analytical approximations and numerical solutions are presented.

2 Review of basic assumptions and simplest case

This section will first summarise the results of [1], dealing with the simplest, one-dimensional equation for space charge and electric field. Next, it will consider aspect related to an ionisation detector used as a time projection chamber (TPC).

2.1 One-dimensional analysis

An ionising particle creates pairs of electrons and positive ions, but because the respective values of drift velocity differ by typically by 5 or 6 orders of magnitude, under steady conditions the density of the two charge carriers differ by the same amount. Therefore, in the fundamental approximation the density of charge is assumed to be due to positive ions alone, ρ^+ , which varies because of the injection of ions from ionising particles, and satisfies the continuity equation

$$\frac{\partial \rho^+}{\partial t} + \nabla \cdot (\rho^+ \mathbf{v}^+) = K . \quad (1)$$

The stationary solution ($\partial \rho^+ / \partial t = 0$) is of interest, and it is determined under the assumption of constant and uniform charge density injection rate K . The value of K depends on the flux of ionising particles crossing the detector and on the value of the electric field, which affects the initial recombination of electrons and ions. The space charge causes a non uniformity in the electric field, and therefore a space dependence of K , which is ignored here, and considered below in Sec. 2.3. The assumption of uniformity and stability of K is valid because the charge injection, due to *e.g.*, cosmic rays, is effectively averaged over the time needed for the ions to drift from anode to cathode. The detector is taken as a parallel-plates ionisation chamber with gap L , operated with voltage V_0 and average electric field $E_0 = V_0/L$ directed

¹On the other side, in gaseous detectors space-charge effects are usually due to ions from multiplication in gas rather than primary ionisation. The subject was discussed first in the context of gas diodes [4, 5], before becoming a subject of relevance in detectors for particle physics [6].

along $+x$, with $x = 0$ ($x = L$) at the anode (cathode). The problem is reduced to one-dimension under the assumption that far from the side wall the border effects are negligible, so that the dependence on y and z may be ignored.

Under these assumptions, and using the mobility coefficient μ^+ , the continuity equation

$$\frac{d(\rho^+ v_x^+)}{dx} = K \quad (2)$$

is solved as

$$\rho^+(x) = \frac{Kx}{\mu^+ E_x(x)}, \quad (3)$$

where $v_x^+ = \mu^+ E_x$ is used and the boundary condition $\rho^+(0) = 0$ is applied, since the positive ions drift away from the anode and no accumulation of space charge is possible at $x = 0$. For $x > 0$, space charge is present reflecting the rate of charge density injection, accumulated over a time effectively equal to $x/(\mu^+ E_x)$.

The electric field satisfies the Gauss's law, which under these assumptions is written as

$$\frac{dE_x}{dx} = \frac{\rho^+}{\epsilon} = \frac{Kx}{\epsilon \mu^+ E_x} \quad (4)$$

and is solved directly as

$$E_x(x) = E_o \sqrt{(E_a/E_o)^2 + \alpha^2 (x/L)^2}, \quad (5)$$

where E_a is the value of the electric field at the anode, which is determined by the boundary $\int E_x dx = V_o$ integrated from anode to cathode, while the adimensional parameter α is defined as [1]

$$\alpha = \frac{L}{E_o} \sqrt{\frac{K}{\epsilon \mu^+}}. \quad (6)$$

This parameter can be interpreted as α^2 being equal to the charge density injection rate K , multiplied by the gap length L and by the ions drift-time across the gap $L/(\mu E_o)$, and divided by the surface charge density $\sigma_o = \epsilon E_o$ at the electrodes, with the last two quantities computed for vanishing K . The ratio $\sigma_o/L \equiv \rho_o$ is the natural unit for evaluating $\rho^+(x)$, which can be written as

$$\rho^+(x) = \alpha^2 \rho_o \frac{E_o}{E_x(x)} \frac{x}{L}. \quad (7)$$

From Eq. 5, and as shown in Fig. 1, the field at the anode E_a is always lower than E_o , while the opposite holds for the field at the cathode E_c . Correspondingly, the electric potential, defined as $V(x) = -\int E_x dx$ and integrated from the anode towards the cathode, deviates from the value $-E_o x$, according to a smooth convex profile. The analytical expression for $V(x)$ is given below in Eq. A.1, Appendix A.

As discussed in [1], a critical situation occurs for $\alpha \geq 2$, when the electric field vanishes at the anode, enhancing recombination between electrons and positive ions.²

As an example, in a liquid argon detector operated at the surface of the Earth, the charge density injection rate due cosmic rays is approximately given by $K = 2 \times 10^{-10} \text{ C m}^{-3} \text{ s}^{-1}$. For $L = 4 \text{ m}$, $E_o = 500 \text{ V/cm}$,

²In the critical condition $\alpha = 2$ the electric field varies linearly as $E_x = 2E_o(x/L)$ and the density of positive ions is uniform: $\rho_c = KL/(2\mu^+ E_o) = 2\rho_o$. For $\alpha > 2$ the active region is reduced to a gap of length $L' = 2L/\alpha$, detached from the anode by $L - L'$, with $E_x = 2E_o(x'/L')$ for $x' = x - (L - L') > 0$, while E_x is highly suppressed for $x \leq L - L'$. The occurrence and the modality of a critical condition, predicted in [1], has been observed in calorimetric cells [3].

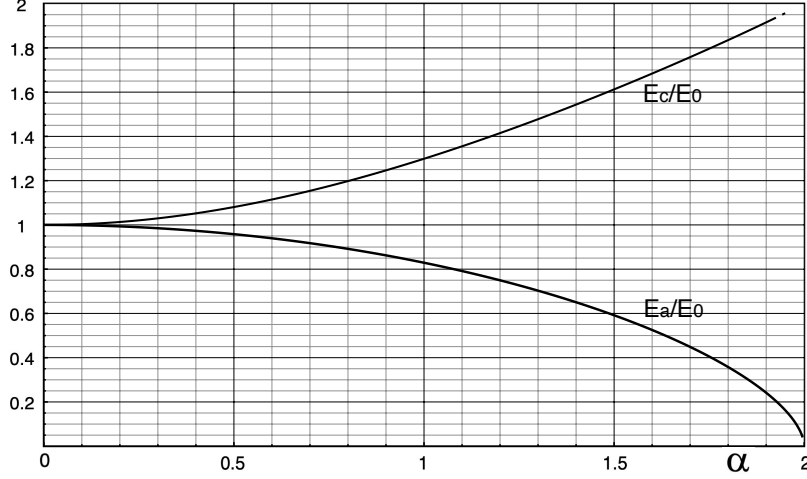


Fig. 1: Normalized electric field at the anode E_a/E_0 and cathode E_c/E_0 as a function of the adimensional parameter α , from reference [1].

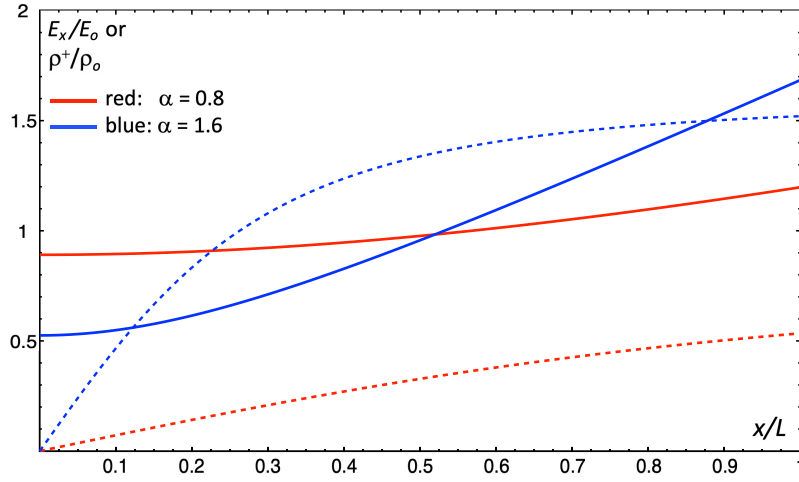


Fig. 2: Electric field (continuous lines) and charge density (dashed line) behaviour for $\alpha = 0.8$ (red) and $\alpha = 1.6$ (blue). The horizontal axis is the drift coordinate divided by the gap length (x/L), with $x = 0(1)$ at the anode (cathode). The electric field is in units of $E_0 = V_0/L$, and the charge density in units of $\rho_0 = \epsilon E_0/L$.

relative dielectric constant of 1.504, and with $\mu^+ = 1.6 \times 10^{-7} \text{ m}^2\text{V}^{-1}\text{s}^{-1}$ for the ion mobility, the adimensional parameter takes the value $\alpha = 0.78$. Figure 2 shows the behaviour of E_x/E_0 and ρ/ρ_0 vs. x/L under similar assumptions. For comparison, the curves corresponding to $\alpha = 1.6$ are also shown.

It should be kept in mind that there is uncertainty in the value of the mobility of Ar^+ ions, with reported values in the range of 0.8 to $2.0 \times 10^{-7} \text{ m}^2\text{s}^{-1}\text{V}^{-1}$ [3, 8, 11, 12, 13], for values of temperature and pressure usual for particle detectors. Such uncertainties propagates directly to the value of the parameter α^2 , and to the application of the results presented in this paper.

Appendix A provides a set of relations valid in first-order expansion in the parameter α^2 , together with numerical approximations at higher order.

2.2 Time projection chambers

In a time-projection chamber, like liquid argon devices designed for neutrino detection [14], the effect of the space charge on the collection time of a charge deposited at a distance x from the anode is described by a time offset δt , given by

$$\delta t(x) = \int_0^x \left(\frac{1}{v^e(x')} - \frac{1}{v^{e_0}} \right) dx', \quad (8)$$

where $v^e(x)$, v^{e_0} are the values of the drift velocity of electrons at the local electric field $E_x(x)$ and at the nominal value E_0 , respectively. Since the electron drift velocity depends monotonically on E_x , the integral receives contribution of different sign from regions of small and large x . Using $t_0 = L/v^{e_0}$ and taking $\delta v^e/v^{e_0} = \gamma(\delta E_x/E_0)$ to describe the non-linearity of the drift velocity of electrons, in the approximation of small values of α it is straightforward to find

$$\delta t(x) \simeq \alpha^2 \frac{\gamma t_0}{6} \frac{x}{L} \left(1 - \frac{x^2}{L^2} \right), \quad (9)$$

which naturally vanishes at $x = 0$ and also at $x = L$, although the latter property holds only to first order in α^2 . The maximum effect on the drift time occurs for $x_{\max} \simeq L/\sqrt{3}$, and is equal to

$$\delta t_{\max} \simeq \alpha^2 \frac{\gamma t_0}{9\sqrt{3}}. \quad (10)$$

The effect on the reconstructed coordinate, which can be referred to as *longitudinal distortion*, is $\delta x = v^{e_0} \delta t$, which in the same approximation has the largest value

$$\delta x_{\max} \simeq \alpha^2 \frac{\gamma L}{9\sqrt{3}} = \frac{\gamma}{9\sqrt{3}} \frac{L^3}{E_0^2} \frac{K}{\epsilon \mu^+}. \quad (11)$$

This equation shows that the longitudinal distortion is proportional to the charge density injection rate and to L^3 , E_0^{-2} . In the example considered above (liquid argon TPC with $\alpha = 0.78$, $L = 4$ m), and using $\gamma \simeq 0.5$ [15], the maximum longitudinal distortion is $\delta x_{\max} \simeq 7.7$ cm.

2.3 Electric field variation and ionisation yield

The analytical description contained in Section 2 can be brought to a more realistic condition by introducing an x dependence in the charge density injection, related to initial charge recombination, which changes the amount of free electrons and ions as a function of the electric field strength. To this purpose K is multiplied by $R(E)$ and, with $E = E_x$, Eq.s 2 and 5 are replaced by:

$$\frac{d(\rho v_x)^+}{dx} = KR(E_x), \quad \frac{dE_x}{dx} = \frac{\rho^+}{\epsilon} = \frac{K \int_0^x R(E_x(x')) dx'}{\epsilon \mu^+ E_x(x)}. \quad (12)$$

Figure 3 shows examples of numerical solutions for $E_x(x)/E_0$. $R(E_x)$ is taken from [16] and normalised to the value for $E_0 = 500$ V/cm: $R(E_x) = 1.15/(1 + 72.9/E_x)$, with E_x expressed in V/cm. Values $\alpha = 0.8$ and 1.6 are considered, including recombination (continuous lines) and excluding it (dashed lines). The difference is negligible for the smaller value of α , and rather small for the larger. The effects of recombination would be more visible for larger values, and the threshold for critical density is increased to $\alpha \simeq 2.5$.

Besides the effect on δx , the x dependence of the field strength needs to be taken into account when the specific energy loss dE/dX along the trajectory of a charged track is extracted from the ionisation signal dQ/dX , for the purpose of particle identification. The local dependence of the charge yield affects the ionisation signal as $dE \propto dQ/R(E(x))$. Furthermore, the segment on the track length $dX = (dx^2 + dy^2 + dz^2)^{0.5}$ requires a *scale correction* for the dx component, proportional to $d(\delta x)/dx$. Using Eq. 9

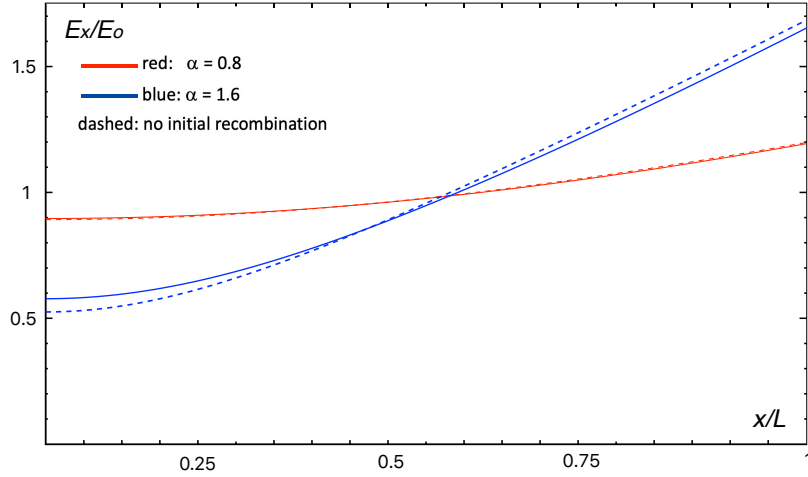


Fig. 3: Normalised electric field $E_x(x)/E_0$ vs. x/L for $\alpha = 0.8, 1.6$, taking into account recombination (continuous lines) and ignoring recombination (dashed lines).

and $\delta x = v_e^e \delta t$, at first order in α^2 the correction varies between $-0.08 \alpha^2 \cos^2 \theta_x$ at the anode to $+0.17 \alpha^2 \cos^2 \theta_x$ at the cathode, where θ_x is the angle between the track segment and the drift direction.

In the following sections, analytical results are obtained ignoring the dependence of the initial recombination on the electric field, while the effect is included in numerical computations.

2.4 Electron attachment and negative ions

Drifting electrons may be captured by electronegative impurities according to $d\rho_e/dt = \rho_e/\tau_e$. The electron lifetime τ_e is related to the attachment rate constant k_e and to the density of electronegative impurities n_i as $\tau_e = 1/(k_e n_i)$. The attachment rate constant depends on the type of impurity, and on the electron energy distribution, which is affected by the electric field, but this dependence has been observed to be rather small for field strength below 1000 V/cm [17].

The continuity equation for the average electron charge density, in steady conditions, can be written as

$$\frac{d(\rho^e v_x^e)}{dx} = -K - \frac{\rho^e}{\tau_e}, \quad (13)$$

where $-K$ this time defines the injection of negative charge density, drifting towards $x = 0$ (with $\rho^e < 0$, $v_x^e < 0$, $K > 0$). An average capture length $\lambda_e = |v_x^e| \tau_e$ can be defined, and compared to the gap length L .

The electron attachment is source of negative ions, which drift towards the anode with a mobility parameter similar to the one of negative ions [12], and contribute to the space charge present in the detector. The result of a numerical solution [18] to the continuity equations for ρ^e , ρ^+ , ρ^- and to the Gauss's law for E_x is shown in Fig. 4 in the case of $\lambda_e(E_0)/L = 2.58$, $\alpha = 1.15$, and assuming equal mobilities for negative and positive ions. The presence of the negative ions causes the minimum of the electric field to move away from the anode to a shallow minimum at $x_{\min}/L \simeq 0.15$, where the field is 3% lower than at the anode; in comparison with the case of infinite lifetime, the field at the anode is increased from $0.77 E_0$ to $0.83 E_0$, and the field at the cathode is barely changed from $1.38 E_0$ to $1.37 E_0$. For an electron lifetime shorter by a factor 2 (*i.e.* $\lambda_e/L = 1.29$), the corresponding value are $x_{\min}/L \simeq 0.24$, $E_{\min}/E_a = 0.94$, $E_a/E_0 = 0.90$, $E_c/E_0 = 1.35$.

An approximate analytical expression for $E_x(x)$, which matches the numerical evaluation at the level of 1%, is provided in appendix B.

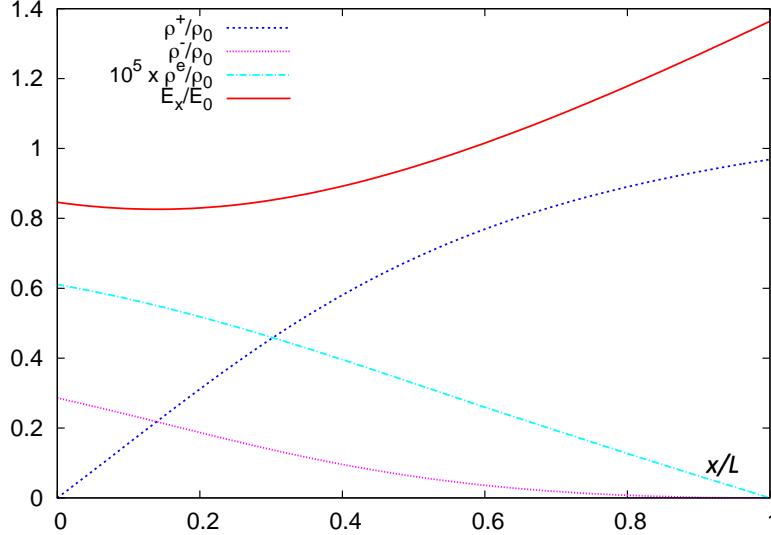


Fig. 4: One-dimensional numerical computation of the effects of electron attachment. The parameters used are $L = 6$ m, $\alpha = 1.15$, equal mobilities $\mu^- = \mu^+$, and $\tau_e = 10$ ms ($\lambda_e/L = 2.58$). The different curves show the absolute values of $E_x(x)$, $\rho^+(x)$, $\rho^-(x)$ and $\rho^e(x) \times 10^5$ vs. x/L , in units of E_0 and ρ_0 .

In the following sections, analytical results are obtained ignoring the dependence of the initial recombination on the electric field, while the effect is included in numerical computations.

3 Dual-phase detectors and feedback of positive ions

Dual-phase scintillation and ionisation detectors have been used for the study of rare processes, and large devices based on argon have been proposed for rare processes and neutrino experiments [19, 20]. After drifting in the liquid, the electrons from primary ionisation are extracted into the vapour phase, where they can be accelerated in order to produce a light signal or to achieve charge amplification [21]. In the latter case, a significant fraction of positive ions from the multiplication process may be fed back to the liquid, contributing to the space charge in the drift volume.

Near the liquid-vapour interface, an extraction grid is designed to establish an electric field strength that facilitates transition of the electrons from the liquid to the vapour. At the interface, dielectric polarisation attracts charges in the vapour phase – of any sign – towards the interface surface, and repels them from the surface when they are in the liquid [22]. The extraction potential for electrons is designed to counteract this effect, together with any effective binding potential for conduction electrons in the liquid phase [23]. It has been argued that the discontinuity of the polarisation field at the interface may prevent positive ions from entering the liquid [19]. Opposite arguments have also been presented [24]. Lacking direct evidence, it is assumed here that positive ions can reach and cross the vapour to liquid interface. Polarisation and binding potential effects appear more likely to play a role in preventing negative ions, which may come from electron attachment, from leaving the liquid phase [25], as they do for electrons. That would be a minor effect under the assumption $\lambda_e \gg L$ and, furthermore, a build-up of negative ions on the liquid-vapour interface would affect more directly the electron extraction from the liquid phase, rather than the electron drift in the liquid TPC.

The relative amount of ions feedback to the drift region is described by the product $\beta = (g - 1) \times f$, where g is the gain on the electron signal and the factor f includes the collection of the positive ions from the amplification region, their transfer into the liquid phase, and the limited transparency of the extraction grid for positive charges. The value of β depends on the electric field at the grid, on the side

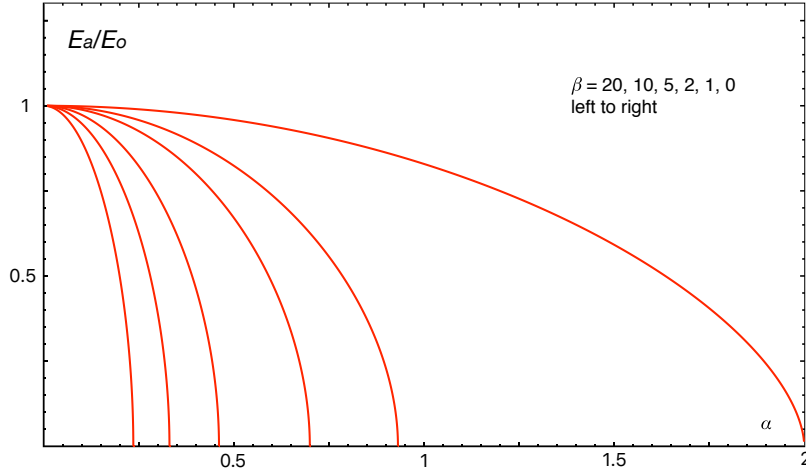


Fig. 5: Behaviour of E_a/E_o vs. α , for different values of the feedback parameter β .

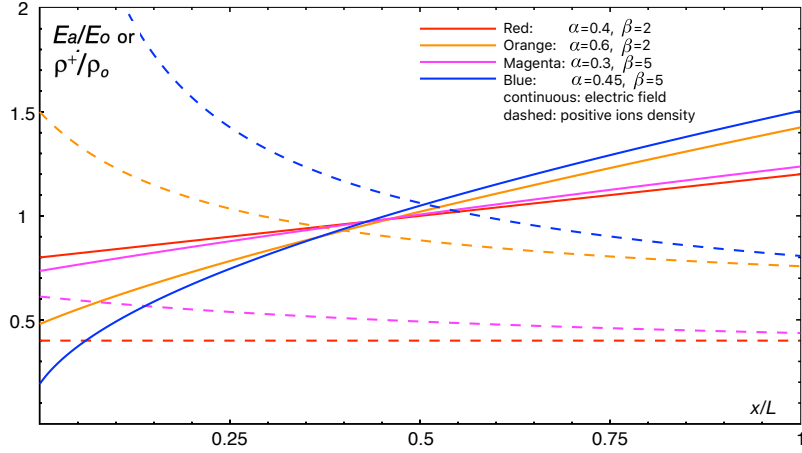


Fig. 6: Behaviour of $E_x(x)/E_o$ (continuous lines) and $\rho^+(x)/\rho_o$ (dashed lines) vs. x/L for different values of the parameters α and β .

of the drift volume, which corresponds to the the field at the anode E_a of single-phase detectors, and is affected by space charge.

In steady conditions, and neglecting electron capture for the moment, the flux of electrons leaving the liquid phase is equal to the total rate of primary ionisation in the detector, $J_e = KL$, and the corresponding flux of positive ions crossing the extraction grid is

$$J(x=0) = \beta KL. \quad (14)$$

The differential equation describing the space charge in steady conditions is the same as Eq. 2, but now the boundary condition includes $J(0)$ and the solution is

$$\mu^+ E_x \rho^+(x) = K(x + \beta L). \quad (15)$$

The differential equation describing the electric field can be easily integrated also in this case, obtain-

ing

$$E_x(x) = E_o \sqrt{(E_a/E_o)^2 + \alpha^2 [(x/L)^2 + 2\beta (x/L)]} . \quad (16)$$

The effect of space charge are now controlled by the two adimensional parameters α and β . The reduction in E_a as a function of α is significantly enhanced by the presence of feedback, as shown in Fig. 5. For $\beta \geq 1$, the critical condition of vanishing E_a is reached for values $\alpha < 1$. Figure 6 shows the behaviour of E_x/E_o and $\rho^+(x)/\rho_o$ for some values of the parameters α and β . While for $\beta = 0$ the space-charge density $\rho^+(x)$ increases with x , the trend may be inverted when ion feedback is present, as shown in these examples.

For detectors with large L/E and feedback of positive ions, natural radioactivity alone may cause non-negligible effects of space charge. With ^{39}Ar radioactivity of about 1.0 Bq/kg in atmospheric argon, $\langle E_\beta \rangle = 220$ keV, effective ionisation potential 24 eV, and ionisation yield of 0.7 at 500 V/cm, the charge injection rate is $K = 1.4 \times 10^{-12} \text{ C m}^{-3}\text{s}^{-1}$. With $L/E = 10 \text{ m} / 500 \text{ V cm}^{-1}$ and $\mu^+ = 1.6 \times 10^{-7} \text{ m}^2\text{V}^{-1}\text{s}^{-1}$, the value $\alpha = 0.16$ is obtained, which implies significant (large) effects of space charge for an ion feedback parameter $\beta > 2$ ($\beta > 20$), as shown in Fig. 5.

4 Mitigation technique n.1 : separation grid

At first order in α^2 , Eq. 4 can be written as $dE_x/dx \simeq (Kx)/(\epsilon \mu^+ E_o)$, so that the difference in field strength between cathode and anode is approximately equal to $(KL^2)/(2\epsilon \mu^+ E_o) \simeq \alpha^2 E_o/2$. This range of variation in field strength can be reduced by means of a third electrode, a grid placed at the coordinate x_g that constrains $V(x_g)$ to a suitable value V_g . The grid generates a discontinuity in E_x that can be exploited to increase the field strength at the anode and decrease it at the cathode. With a higher field on the anode side of the grid, drifting electrons will cross it, while a fraction of positive ions are captured, reducing further the effects of space charge in the region between the grid and the cathode.

Figure 7 illustrates the value of $E_x(x)/E_o$ for a given configuration of x_g and $V(x_g)$, and different conditions of space charge, corresponding to α equal to 0.8, 1.6 and 2. The grid reduces by at least a factor 2 the range between the highest and the lowest values of the field strength across the full gap. Figure 8 shows the corresponding distribution of $\rho^+(x)/(\rho_o)$. For $x < x_g$, the electric field is described by Eq. 5 as in the case without grid, but now the boundary condition on the field at the anode E_a is

$$\int_0^{x_g} \sqrt{(E_a/E_o)^2 + (\alpha x/L)^2} dx = \delta_g V_o , \quad (17)$$

with $\delta_g = -V_g/V_o$ and, as usual, $V = -V_o$ (0) at the cathode (anode). The boundary condition can be written as

$$\int_0^1 \sqrt{\left(\frac{E_a x_g}{E_o \delta_g L}\right)^2 + \left(\frac{\alpha x_g^2 x'}{\delta_g L^3}\right)^2} dx' = L , \quad (18)$$

with $x' = x \times L/x_g$.

As discussed below, a convenient configuration is with $x_g/L = \delta_g$, in which the grid restores at x_g the voltage that would be obtained without charge injection. Then the boundary condition becomes

$$\int_0^1 \sqrt{(E_a/E_o)^2 + (\alpha x_g x'/L^2)^2} dx' = L , \quad (19)$$

showing that E_a , together with $E_x(x)$ for $0 < x < x_g$, reproduces the solution for $0 < x < L$ obtained in the case without grid and with α replaced by $\alpha \times x_g/L$. Therefore, the distortion to the values of the electric field are reduced by a factor equal to the square of x_g , and the longitudinal distortion in a TPC device by the cube of x_g .

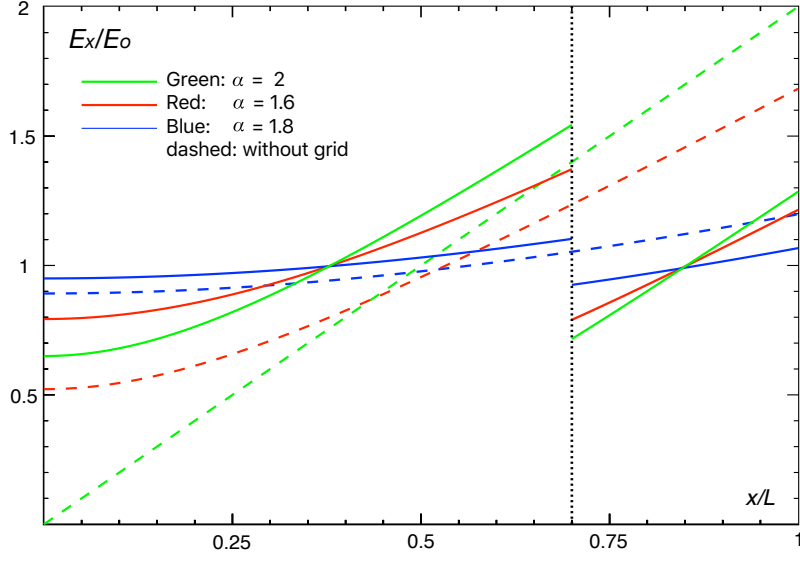


Fig. 7: Behaviour of $E_x(x)/E_0$ with a voltage grid placed at $x = 0.7L$, with $\alpha = 0.8$ (blue), 1.6 (red), and 2.0 (green). The voltage at the grid is set at the value corresponding to a condition of no space charge ($\delta_g = x_g/L$). For comparison, the dashed lines show the electric field without voltage grid.

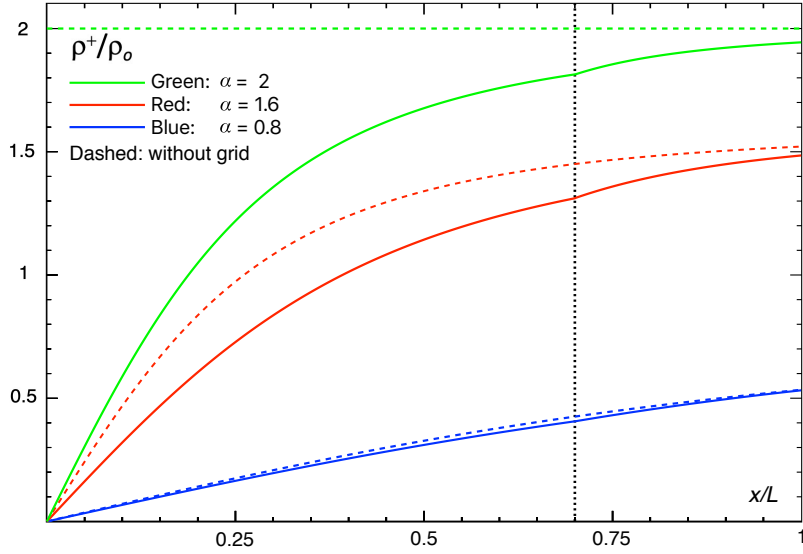


Fig. 8: Behaviour of $\rho^+(x)/\rho_0$ with a voltage grid placed at $x = 0.7L$, with $\alpha = 0.8$ (blue), 1.6 (red), and 2.0 (green). The voltage at the grid is set at the value corresponding to a condition of no space charge ($\delta_g = x_g/L$). For comparison, the dashed lines show the space-charge density without voltage grid.

As shown in appendix C, for $x > x_g$, the general solution for the $E_x(x)$ is

$$E_x(x) = E_0 \sqrt{(E_{g+}/E_0)^2 + \alpha^2[(x - x_g)^2/L^2 + 2(E_{g+}/E_{g-})x_g(x - x_g)/L^2]} \quad (x > x_g), \quad (20)$$

where E_{g-} and E_{g+} are the field values at the grid, on the sides of $x < x_g$, $x > x_g$ respectively, and are determined by the values of x_g and δ_g , together with those of E_0 and α . The flux of positive ions ρ^{+v+} is

reduced by the factor E_{g+}/E_{g-} as it crosses the grid. The same factor applies for the change in ion drift velocity, so that derivative dE_x/dx and the density ρ^+ are continuous across the grid, as shown in Figs 7 and 8.

The parameter x_g and δ_g can be chosen so that in the two regions defined by the grid, the ranges in the value of E_x are approximately equal. This is approximately equivalent to aiming at the maximisation of the lowest value of E_x across the full gap. As discussed in more detail in appendix C, choosing $\delta_g = x_g/L$, *i.e.* restoring at x_g the voltage that would be obtained without space charge and without grid, brings in proximity of the optimal configuration, and may result of practical implementation. The optimal value of x_g/L is in the approximate range 0.6–0.7, with limited sensitivity to the exact value, apart from a preference for the lower (higher) values for α larger (smaller) than 1.

As shown in Fig. 7, the grid changes the range of $E_x - E_o$ by a factor approximately equal to $(x_g/L)^2 \simeq 0.5$. The effect is larger when critical conditions are approached: for $\alpha = 2$, the grid reduces the electric field variation from $\pm 100\%$ to about $\pm 30\%$.

As a final remark, the separation grid is charged with negative surface charge density $\sigma_g = -\varepsilon(E_{g-} - E_{g+})$ and subject to the electrostatic pressure $p_g = -\varepsilon(E_{g-}^2 - E_{g+}^2)/2$. To first order in α^2 , the pressure is given by the expression $p_g \simeq -0.24\varepsilon E_o^2 \alpha^2$, which is accurate within 5% for the examples shown in Figs 7 and 8. In practical situations it may be similar to the pressure on the anode ($p_a \simeq 0.5\varepsilon E_o^2(1 - \alpha^2/3)$), and is smaller than the pressure on the cathode ($p_c \simeq -0.5\varepsilon E_o^2(1 + 2\alpha^2/3)$).

5 Side walls, field cage and transverse effects

Besides the effect on the component of the electric field driving the drift of electrons and ions discussed above, which can be referred to as *longitudinal*, in practical conditions the space charge can induce *transverse* distortion. The main reason for this effect is that liquid-argon time-projection chambers [7, 8] have been operated with side walls equipped with field-cages designed for the operation without space charge, *i.e.* with a uniform gradient of the voltage V_{fc} established by the field cage ($dV_{fc}/dx = -E_o$). This field pattern does not match the field established far inside from the field cage, and a transverse component of the electric field arises close the side walls.

A constraint on the transverse components of the electric field E_y, E_z can be placed considering line-integrals $\oint \vec{E} \cdot d\vec{s}$ computed along closed paths. For the component along y , consider the path of four straight segments shown in Fig. 9, which starts at a point (x, y, z) far from the field cage, (a) reaches the field-cage at $(x, 0, z)$, (b) reaches the anode at $(0, 0, z)$, (c) follows the anode to $(0, y, z)$, and (d) closes the path to (x, y, z) . The contribution from (c) is null, so that the opposite of the term in (a) is equal to the sum of the term in (b) and (d), and satisfies on the line-integral condition

$$\begin{aligned} \int_{(x,0,z)}^{(x,y,z)} E_y(x, y', z) dy' &= \int_{(x,0,z)}^{(0,0,z)} E_x(x', 0, z) dx' + \int_{(0,y,z)}^{(x,y,z)} E_x(x', y, z) dx' \\ &= -E_o x - V(x, y, z) \\ &\simeq -E_o x - V(x), \end{aligned} \quad (21)$$

where the electric voltage at the field-cage is $-E_o x$, the dependences of $V(x, y, z)$ on y, z can be neglected because of the distance from the field cage, and $V(x)$ is the electric voltage in the one-dimensional description of space-charge effects obtained from the integration of $-E_x(x)$ in Eq. 5. Since for $0 < x < L$ the absolute value of $V(x)$ is smaller than $E_o x$, the transverse electric field is negative (directed towards the field cage), and the drifting electron are focussed toward the center of the detector. The value of $V(x)$ and its approximation to first order in α^2 are provided in Appendix A. For $\alpha < 1.5$, the absolute value of the integral is largest at $x \simeq L/\sqrt{3}$ and is approximately equal to $0.064 \alpha^2 E_o L$. For α approaching 2, the maximum is moved towards $x \simeq L/2$ with the value $0.25 E_o L$.

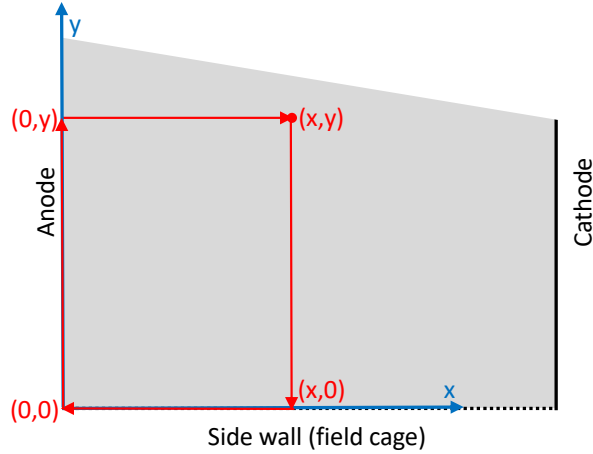


Fig. 9: Path for line integral of electric field, as discussed in the text.

The solution of a set of dependent differential equations describing the electric field and the motion of charge species can be numerically approximated using FEA software [18]. Computations have been made in three dimensions, or in two dimensions when the third coordinate is far from the field cage. Figure 10 shows an example of contours of equal values of E_x and E_y in a two dimensional computation. If the transverse size of the detector is large compared to the anode to cathode distance L , the fundamental parameters that define the electric field are the same as in the one-dimensional case: E_o , L , and α^2 , with the latter proportional to $(L/E_o)^2$. Therefore, $(E_x - E_o)/E_o$ and E_y/E_o scale as α^2 , and L^2/E_o^2 , spatial distortions δx , δy in a TPC detector scale as $\alpha^2 L$, and L^3/E_o^2 , when all quantities are computed on coordinates that scale as x/L and y/L . Numerical computations show that these scaling relations remain valid also for finite electron lifetime, if $\lambda_e \equiv |v^e(E_o)|\tau_e \gg L$.

On the side wall ($y = 0$), *i.e.* on the field-cage, the largest value of of the transverse component $|E_y|$ occurs for $x \simeq 0.63L$, and is equal to about $0.18\alpha^2 E_o$. Equation A.6 in Appendix A provides a polynomial approximation of the transverse component of the electric field at the field cage ($E_y(x,0)$). The transverse component decreases with y/L , following approximately the exponential dependence $E_y(x,0) \times \exp[-y/\lambda_y(x)]$, with $\lambda_y(x) \simeq 0.47[1 - 0.5(x/L - 0.5)]L$.³ At a distance from the side wall equal to 0.5 (1.0) L , the maximum value of the transverse field occurs at $x \simeq L/2$ and is equal to about 4.1% (1.1%) of $\alpha^2 E_o$.

At the field cage, the longitudinal component $E_x(x,0)$ is constrained to E_o . For $y > L/2$ and $x \simeq L/2$, $E_x(x,y)$ is described by the one-dimensional approximation (Eq. 5) within about 1%. Near the electrodes, the one-dimensional approximation is valid for $y > L$ to the same accuracy.

A finite electron lifetime, if significantly larger than the electron maximum drift time, does not alter the scenario, as shown in the comparison of Figs. 10 and 11. The latter is obtained from a numerical calculation using $\lambda_e^e/L = 2.58$. As discussed above in Sec. 2.4, the presence of negative ions reduces the distortion in E_x (the range -22% to $+38\%$ is reduced to -17% to $+34\%$ for $\alpha = 1.15$, with the minimum of E_x moved to $x \simeq 0.15$). The maximum values of $|E_y|$ is reduced by about 10%. The lateral extension of the region with significant transverse field is not significantly modified.

The ionisation electrons drift following the direction of $-\bar{E}$, and the transverse component E_y causes a

³This value is obtained from the ratio $\lambda_y = [V(x) - E_o x]/E_y(x,0)$, with $V(x)$ from the one-dimensional model and $E_y(x,0)$ from the polynomial fit. A better approximation to $E_y(x,y)$ for $x \simeq L/2$ is provided in Eq. A.9.

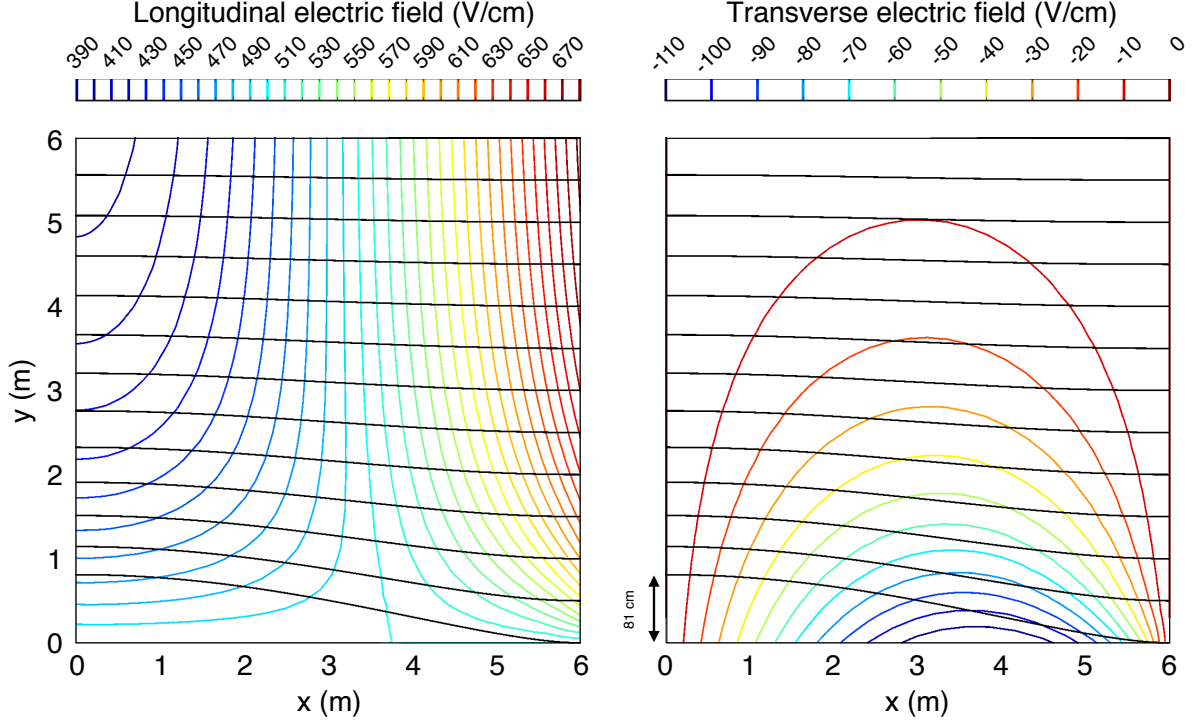


Fig. 10: Contours of equal values of the longitudinal E_x (left) and transverse E_y (right) components of the electric field from a numerical calculation. The plots cover the anode to cathode region, 6 m long, and a 6 m wide region with the field cage at $y = 0$. The computation neglects dependences on the third coordinate z , and assumes a detector transverse size of 20 m along y . Input values are $E_o = 500$ V/cm and $\alpha = 1.15$. The contours cover the range of E_x from 390 to 670 V/cm, and of E_y from 10 to 110 V/cm. The black line shows the drift path of electrons from the cathode to the anode.

displacement of the point of collection of the electrons originated in (x, y, z) according to the expression

$$\delta y(x, y, z) = \int_{(x, y, z)}^{x=0} \frac{E_y}{E_x} dx, \quad (22)$$

with the integration computed along the path followed by the drifting electrons. Under usual conditions, this *transverse distortion* collects same-sign contributions along the full drift path, and for an initial coordinate $x > L/2$, its value can be significantly larger than the longitudinal distortion of Eq. 11, because the latter is reduced by competing contributions of different sign from the regions $x \gtrsim L/2$ and $x \lesssim L/2$, and also the reduced dependence of the electron drift velocity on the electric field ($\gamma = (\delta v^e / v^e) / (\delta E_x / E_o) \simeq 0.5$ for $E_o \simeq 500$ V/cm). The largest transverse distortion occurs for drift path originating at $x = L$ and $y = 0$, where the numerical computation provides $\delta y_{\max} = \delta y(L, 0, z) = 0.105 \alpha^2 L$, which is three times larger than the corresponding maximum longitudinal distortion (the coordinate z is assumed here to be far from the corresponding side walls). Drift paths are shown as black lines in Figs 10 and 11.

The transverse distortion $\delta y(x, y, z)$ reflects into a scale distortion along the y direction equal to $d(\delta y)/dy$, which should be taken into account for measurements of specific signal yield dQ/dX , or when establishing intervals on the y coordinate. The largest distortion to the length scale dX occurs at the cathode and is approximately equal to $-0.2 \alpha^2 \exp(-2y/L) \cos^2 \theta_y$, where θ_y is the angle between the direction of dX and the y axis.

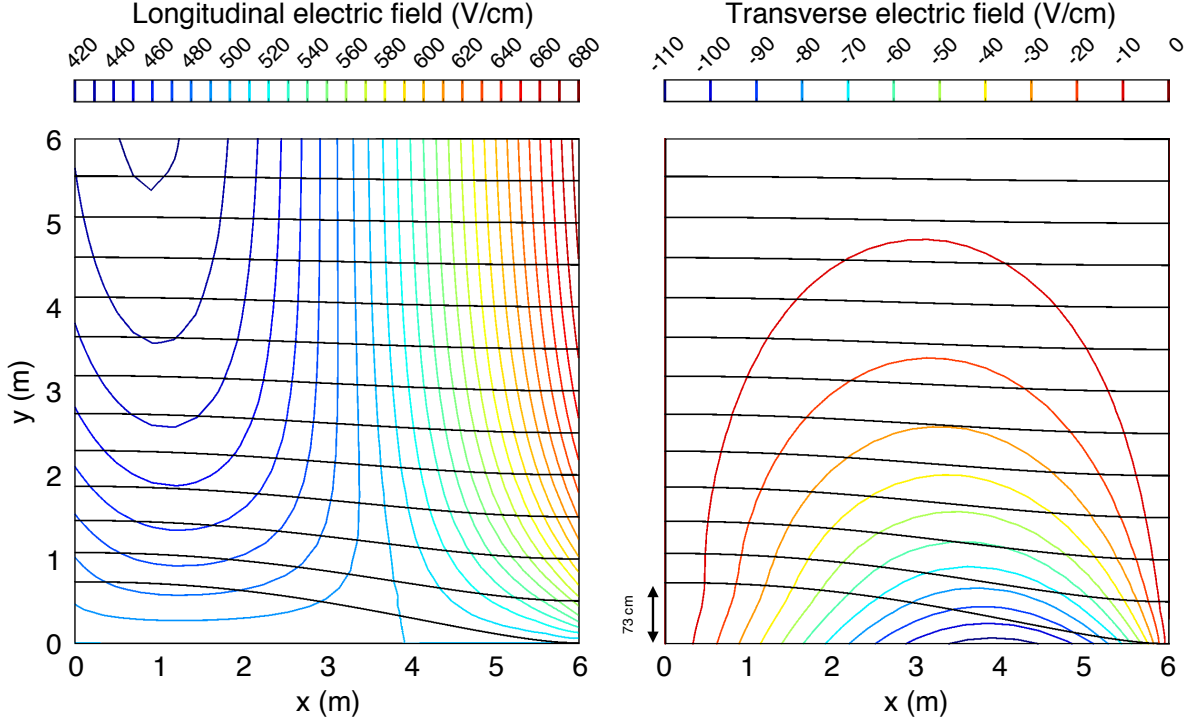


Fig. 11: Same as in Fig. 10, but now with electron attachment corresponding to $\tau_e = 10$ ms, and equal mobility for positive and negative ions.

6 Detector aspect ratio

If the transverse size of the drift volume (with widths W_y , W_z) is not much larger than the drift gap L , the one-dimensional description of sections 2–4 needs to be revised. General features and numerical examples are presented in this section.

As discussed in section 5, with $L \ll W_z$ and for the z coordinate far from the edges $z = 0, W_z$, the transverse component of the electric field decreases as $E_y(x, y) \approx E_y(x, 0) \times \exp(-y/\lambda_y(x))$ as the distance y from the field cage increases, with $\lambda_y \simeq L/2$. If W_y is not much larger than L , there is not enough width to reach a negligible value of E_y before approaching the centre of the drift volume $y \simeq W_y/2$. Because of symmetry with the other half of the detector, E_y still vanishes at $y=0$, but does it with a finite gradient

$$E_y(x, y) \simeq \kappa(x) \times (y - W_y/2) \quad (y \simeq W_y/2). \quad (23)$$

The parameter κ vanishes at the electrodes ($x = 0, x = L$), and is a first order quantity in α^2 in the range $0 < x < L$.

Table 1 shows the result of a numerical computation of $\partial E_y/\partial y$ for different detector aspect ratios, at coordinates $x/L = 0.5$, $y/W_y = 0.125, 0.25, 0.5$, for $\alpha = 1.15$, $E_o = 500$ V/cm, $\tau_e = 10$ ms, and equal mobility of positive and negative ions. The dependence on z is ignored in the first three rows ($W_z \gg L$ and $L < z < W_z - L$), while in the last row $W_z = L$ and the gradient is shown at $z = W_z/2$, where $\partial E_z/\partial z = \partial E_y/\partial y$.

Because of $\partial E_y/\partial y$, $\partial E_z/\partial z$, the Gauss' equation for the main component $\partial E_x/\partial x$ used in Section 2 is modified. For a detector with $W_z = W_y = W$, near the axis $y = z = W/2$, both transverse component of the electric field contribute equally:

$$\frac{\partial E_x}{\partial x} = \frac{\rho}{\epsilon} - \frac{\partial E_y}{\partial y} - \frac{\partial E_z}{\partial z} \simeq \frac{\rho}{\epsilon} - 2\kappa \quad (y \simeq z \simeq W/2). \quad (24)$$

Table 1: Gradients of the transverse electric field $\partial E_y/\partial y$ for different values of y and different detector geometries, computed numerically at $x = 3$ m, $z = W_z/2$, for $\alpha = 1.15$ and $\tau_e = 10$ ms. In the Gauss' equation for $\partial E_x/\partial x$, the transverse gradient is subtracted from the charge density $\rho/\epsilon \simeq 0.53$ V cm⁻². In the last row, the gradient $\partial E_z/\partial z$ contributes an equal subtraction.

$L \times W_y \times W_z$	y=3 m	y= 6 m
$6 \text{ m} \times 24 \text{ m} \times \infty$	$\partial E_y/\partial y = 0.12 \text{ V cm}^{-2}$	$\partial E_y/\partial y = 0.026 \text{ V cm}^{-2}$
$6 \text{ m} \times 12 \text{ m} \times \infty$	$\partial E_y/\partial y = 0.12 \text{ V cm}^{-2}$	$\partial E_y/\partial y = 0.052 \text{ V cm}^{-2}$
$6 \text{ m} \times 6 \text{ m} \times \infty$	$\partial E_y/\partial y = 0.22 \text{ V cm}^{-2}$	
$6 \text{ m} \times 6 \text{ m} \times 6 \text{ m}$	$\partial E_y/\partial y = 0.17 \text{ V cm}^{-2}$	

Both ρ/ϵ and κ are positive and first order in α^2 , so that κ , which is due by the relative proximity of the linear field-cage, reduces the effects of space charge at the center of the detector.⁴ The values shown in Table 1 should be compared to ρ/ϵ , which is equal to about 0.53 V cm⁻² at the center of the drift volume. Using the Gauss' equation, the different configurations shown in the table correspond to a reduction of $\partial E_x/\partial x$ at the center of the drift volume, compared to the value obtained for $L \ll W_x, W_y$, in the range of 10 to 65%.

The values of $\partial E_y/\partial y$ shown in Table 1 can be scaled to different intensities taking into account that they are proportional to α^2 . Furthermore, for $L = W_y \ll W_z$ or $L = W_y = W_z$, and $\lambda_e \gg L$, the gap L is effectively the only parameter with the dimension of length, so that at the center of the detector:

$$\kappa(L/2) = 0.20 \alpha^2 E_o/L, \quad (L = W_y \ll W_z) \quad (25)$$

$$\kappa(L/2) = 0.15 \alpha^2 E_o/L. \quad (L = W_y = W_z) \quad (26)$$

In the latter case, $\partial E_y/\partial y$ is smaller because the amplitude of $E_y(x, y, z)$ is reduced by the constraints $E_y(x, y, 0) = E_y(x, y, W_z) = 0$ imposed by the field cage. However, the term $\partial E_z/\partial z$ enters as well in Eq. 24. Naturally, the boundary conditions are more effective in reducing the effects of space charge when both lateral dimensions are comparable to the gap length. Analytical approximations to $\kappa(x)$ are provided in Eq.s A.7, A.8 in Appendix A, together with approximations of the y dependence of E_y .

The numerical computation of the field strength along the drift direction is illustrated in Fig. 12, for a drift volume with $L = W_y = W_z = 6$ m. The contours of equal values of E_x are shown on the symmetry plane $z = 3$ m, and on the plane $z = 0.5$ m. The plot for $z = 3$ m can be compared to Fig. 11-left. The proximity with the field cage in both y and z reduces the range of E_x on the detector symmetry axis to about 460–610 V/cm, a factor 0.6 smaller than in the case of large detector widths. At a $z = 0.5$ m the range of E_x is reduced by an additional factor 0.5.

The narrow aspect ratio has a smaller impact on on the lateral distortion, since δy is determined dominantly by the closest field cage. The comparison of Fig.s 12-left and 11 shows a 16% reduction in $\delta y(x, 0, z)$ at $z = 3$ m.

Table 2 shows the comparison of different geometries, providing the extremes values for E_x (on the detector axis, or far from the side walls), the maximum transverse component of the electric field $|E_y(x, 0, z)|_{\max}$, and the maximum transverse shift of an electron path $\delta_y(L, 0, z)_{\max}$. The numerical values are provided showing explicitly the dependence on the scaling variables α, L , and can be applied to different configurations, with relative accuracy of some per cent for $\alpha < 1.5$. The table also shows the

⁴The continuity equation for the space-charge density is also affected by the parameter κ , but less directly than E_x . Near the detector axis and considering positive ions, the transverse components of the current density satisfy $\rho^+ v_y^+ \simeq \rho^+ \mu^+ \kappa (y - W_y/2)$, and similarly for $\rho^+ v_z^+$. The gradient of ρ^+ vanishes along the y, z directions, so that the continuity equation becomes $\partial_x(\rho^+ E_x) \simeq K/\mu^+ - 2\kappa \rho^+$. The second term on the right reduces the amount of space charge stored in the detector, but it contributes at order α^4 , with limited effects unless α approaches the critical value. The same conclusion holds if negative ions are taken into consideration.

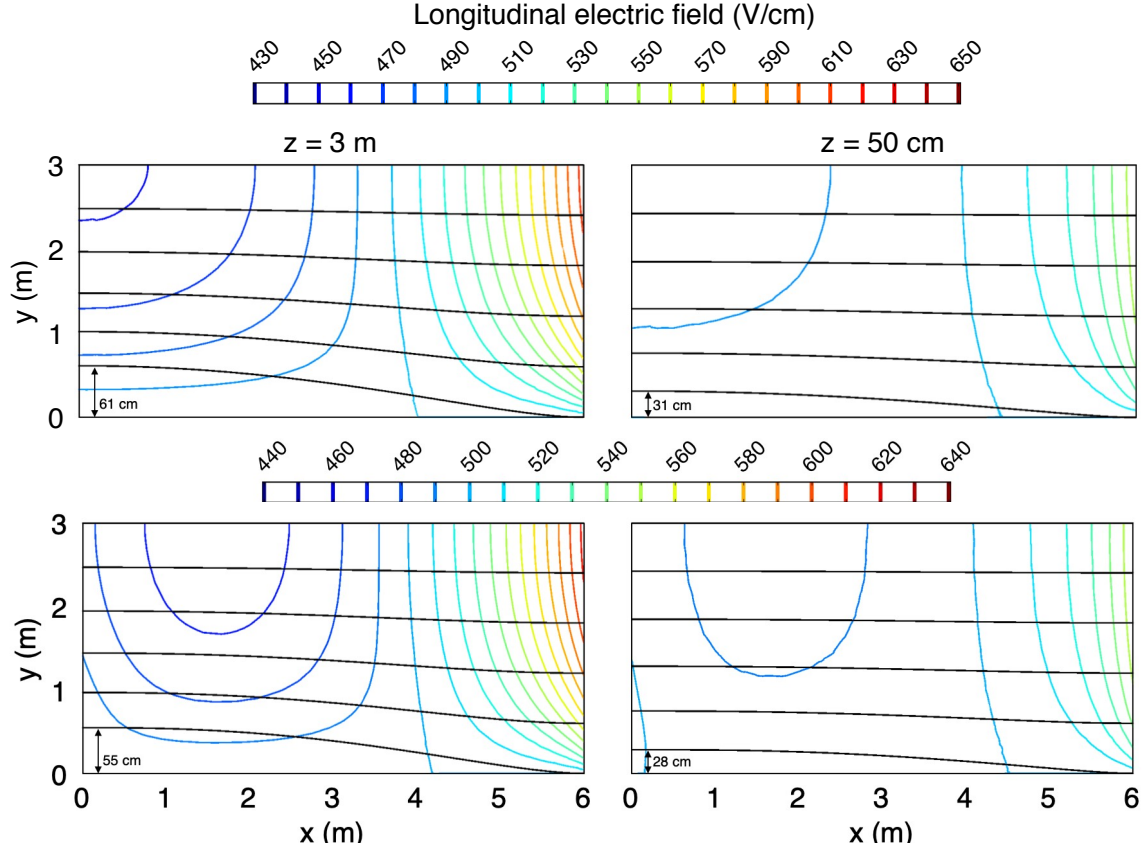


Fig. 12: Contours of equal value of E_x and drift paths projected on the (x, y) plane, for a cubic detector with 6 m sides, with $E_o = 500$ V/cm and $\alpha = 1.15$. The plots on the top are obtained under the assumption of infinite electron lifetime, those on the bottom for $\tau_e = 10$ ms, to be compared to a drift time across the full gap of about 3.9 ms. The plot on the left are for the symmetry plane $z = 3$ m, those on the right for $z = 0.5$ m.

Table 2: Comparison of different geometries of the drift volume: (a) $L \ll W_y, W_z$ and $\tau_e \gg 10$ ms; (b) $L \ll W_y, W_z$, $\tau_e = 10$ ms; (c) $L = W_y = W_z$, $\tau_e = 10$ ms; (d) $L = W_y = W_z$, $\tau_e = 10$ ms and positive ions feedback parameter $\beta = 1$. The results in columns (e), (f) refer to $L = W_y = W_z$ with the correction to the field cage discussed in Sec. 7, with $\tau_e = 10$ ms, and with $\beta = 1$ for column (f). The computation is made for $L = 6$ m, $\alpha = 1.15$.

	(a)	(b)	(c)	(d)	(e)	(f)
$(E_x/E_o - 1)_{\min} \times \alpha^{-2}$	-17%	-13%	-5%	-36%	-9%	-49%
$(E_x/E_o - 1)_{\max} \times \alpha^{-2}$	29%	28%	17%	29%	22%	41%
$ E_y/E_o _{\max} \times \alpha^{-2}$	18%	17%	14%	29%	10%	22%
$\delta y_{\max} \times \alpha^{-2} L^{-1}$	10%	9%	7%	16%	4.0%	11%

result for a detector of equal sides ($L = W_y = W_z$), including the case of positive ions feedback parameter $\beta = 1$, and the effect of the mitigation procedure discussed in Sec 7.

7 Mitigation technique n.2 : corrections to HV field-cage

The transverse components E_y, E_z can be cancelled by means of setting the voltage gradient on the field-cage $V_{fc}(x)$ so that it reproduces the voltage profile $V(x)$ corresponding to the one-dimensional description of the effects of space charge. In that condition, the field-cage is just as effective in removing

border effects as the usual configuration of uniform gradient does for the case of $\alpha \ll 1$.

However the accuracy of the tuning $V_{fc}(x)$ is limited by different factors. Firstly, one has to rely on an *a priori* rather accurate knowledge of the ratio of charge density injection and ion mobility K/μ^+ , which includes the effect of ionisation yield and determines the value of α . A reasonable estimation of the electron lifetime τ_e is also needed, if λ_e is not much larger than L . Secondly, as discussed below in Sec. 8, convective motion related to thermal gradients and to fluid recirculation may affect significantly the distribution of space charge, introducing additional dependences on x, y and z , and preventing an accurate cancellation of the transverse components of the electric field.

Because of these inherent difficulties, an approximate correction to the voltage profile of the field cage is discussed here: besides the voltage imposed at the anode ($V_{fc}(0) = 0$) and cathode ($V_{fc}(L) = -V_o$), a third connection is provided to a resistive field cage at a coordinate $x_{fc} \simeq L/2$, where the voltage is set a value V_{fc} with absolute value lower than $V_o \times (x_{fc}/L)$ and closer to the voltage $V(x_{fc})$ observed at the same distance from the electrodes and far from the field cage. The voltage profile on the field cage remains linear, but with a change of slope at $x = x_{fc}$. Differently from the usual configuration, where the drifting electrons are attracted inward along the entire drift gap, and in particular for $x \simeq x_{fc}$, now the transverse component of the electric field is cancelled in the region where it was largest, and the remaining component at $x \simeq x_{fc}/2$ and $x \simeq (x_{fc} + L)/2$ have smaller amplitude.

The value of V_{fc} can be considered as adjustable to the actual conditions of α , V_o and, to some extent, to the effects of convective motion in which the TPC is operated, in particular if independent values of V_{fc} can be chosen for four sides of the field-cage.

Figure 13 shows the result of a numerical computation for a detector with $L = 6$ m, $E_o = 500$ V/cm, and large width, like in Fig. 11. The (x, y) projection of the equipotential contours and of the drift paths are shown for the usual field cage, and for a correction applied at $x = 3.6$ m, where the voltage is set at -159 kV rather -175 kV. In this way, the transverse component of the electric field is locally cancelled. The maximum transverse distortion of a drift path across the full gap is reduced by a factor 2, which applies also at larger y values. The corresponding contours of equal E_x and E_y are shown in the bottom plots, which may be compared to those of Fig. 11.

For a narrow aspect ratio $L \lesssim W_y$ or W_z , as discussed in Section 6 the voltage profile established by the field cage affects the electric field across the entire detector volume. The correction to the field cage has the desirable effect of reducing the transverse components of the electric field, achieving a more uniform detector response in the plane y, z . On the other hand, it increases the range of the x -dependent effects, with a larger reduction in E_x in the region of the anode and a larger increase at the cathode. The effect is shown in Fig. 14-top, which may be compared to Fig. 12. A correction at $x = 3.5$, with a reduction of the voltage from -175 kV to -161 kV, reduces the maximum transverse distortion by a factor 2, but the range in the longitudinal component at $z = 3$ m is increased by a factor 1.5.

A dual-phase detectors with feedback of positive ions requires larger corrections in order to cancel locally the transverse component of the electric field. Figure 14-bottom shows the case with $\beta = 1$, with the voltage at $x = 3.5$ raised to -141 kV. The comparison with Fig. 15 shows a reduction in the maximum transverse distortion by a factor 0.71, but an increase the range of variation of the longitudinal component of the electric field by a factor 1.4. The comparisons among different configurations are summarised in Table 2.

In the examples shown in Fig.s 13–14, the correction to the field cage is chosen aiming at a compensation of the transverse component of the electric field at $x = x_{fc}$ and y, z in proximity of the field cage. A over-compensation, with a larger correction to $V(x_{fc})$, may be used to invert locally the sign of the transverse component, obtaining a further reduction of the value δy_{max} for the full drift from anode to cathode. The limit to this option is posed the loss of drifting electrons from primary ionisation for $x \gtrsim x_{fc}$ and

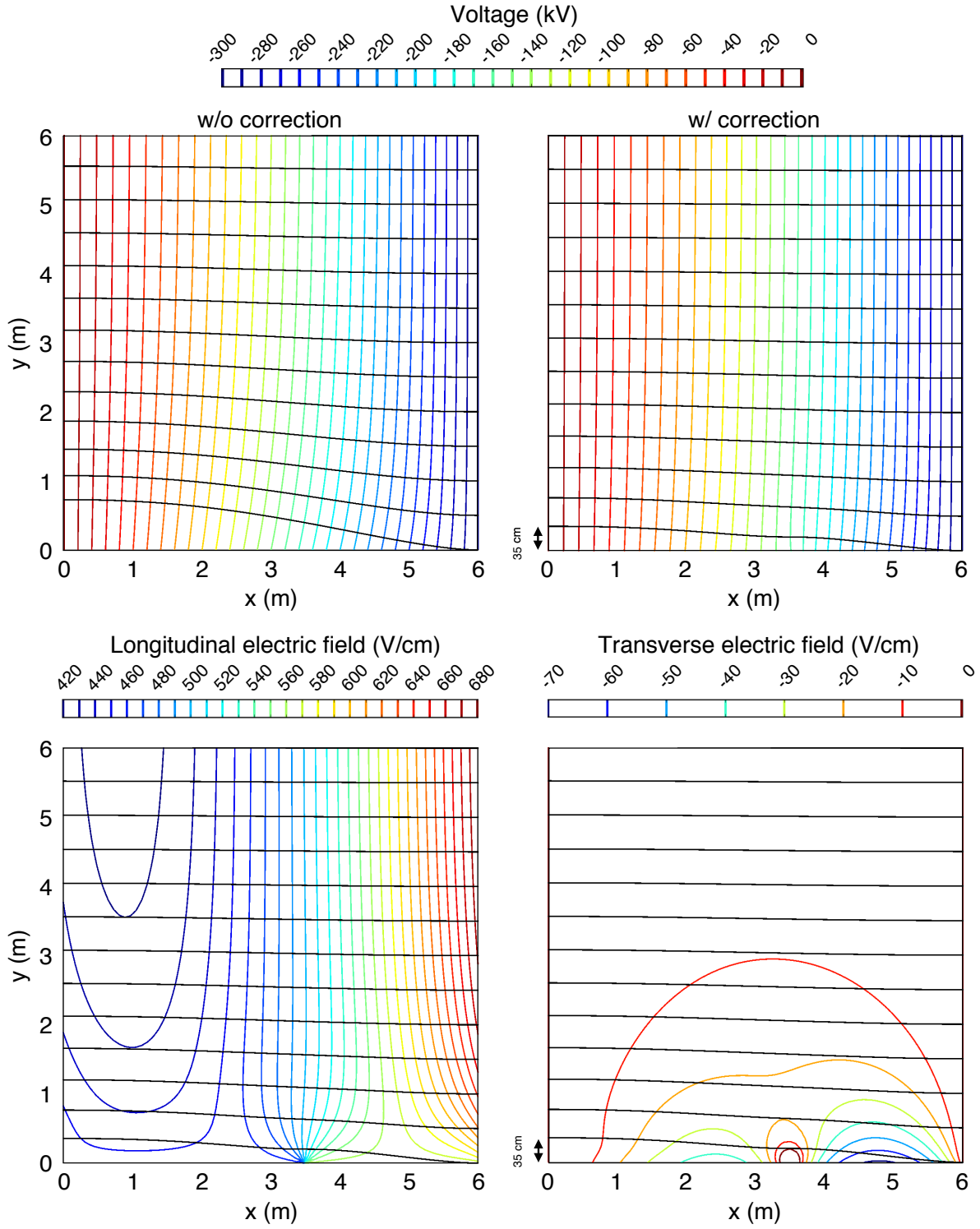


Fig. 13: Contours of equal voltage $V(x,y)$ and drift paths, with a usual voltage gradient at the field cage (*top left*), and with a third voltage connection at $x = 3.5$ m, as discussed in the text (*top right*). The plots on the bottom show the contours of equal $E_x(x,y)$ and equal $E_y(x,y)$ respectively, and drift paths, with the correction applied to the field cage. The applied voltage is $V_o = 300$ kV, $\alpha = 1.15$, and the width along y is much longer than the gap length $L = 6$ m.

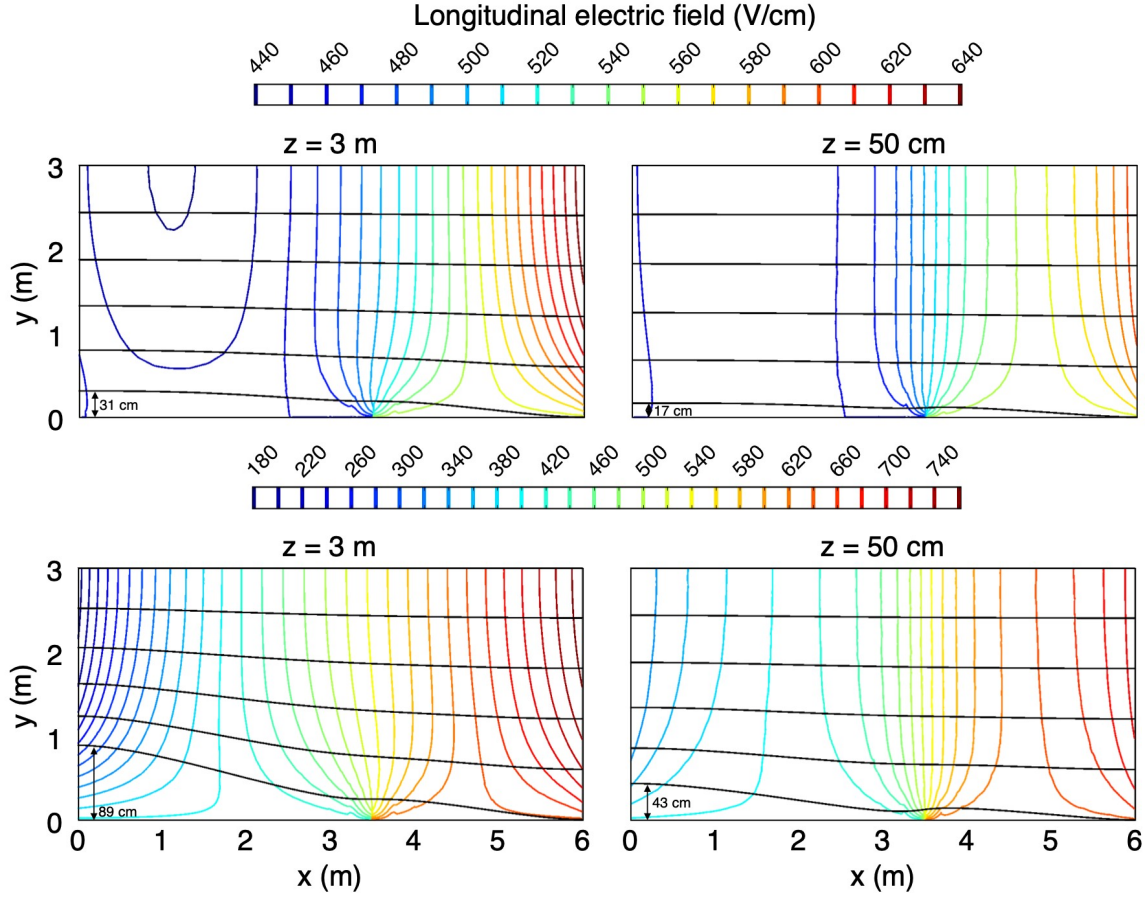


Fig. 14: Contours of equal value of E_x and drift paths projected on the (x, y) plane, for a cubic detector with 6 m sides, with $E_o = 500$ V/cm and $\alpha = 1.15$, with a correction applied to the field cage at $x = 3.5$ m. The plots on the bottom are computed with a positive ions feedback parameter $\beta = 1$. The plots on the left are computed for $z = 3$ m, those on the right for $z = 0.5$ m.

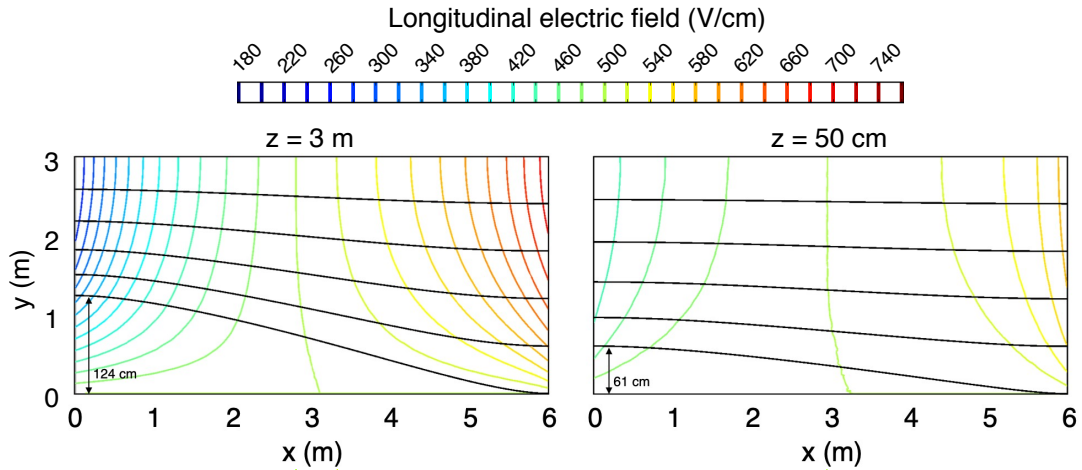


Fig. 15: Contours of equal value of E_x for a cubic detector, as in Fig. 12, with $\tau_e = 10$ ms and with positive ions feedback parameter $\beta = 1$.

sufficiently close to the field cage, which are driven outward and may be captured on the field cage without reaching the region $x \simeq x_{fc}/2$, where they would be driven inward. If the active region at the anode starts at a distance Δy from the field cage, a convenient design solution is to use an over-correction for which the maximum local outward displacement of drifting electrons matches the value of Δy .

Considerations on the optimal values for position x_{fc} and the voltage $V(x_{fc})$ are presented in Appendix D.

For a detector with a narrow aspect ratio, and in particular in the case of feedback of positive ions, a more effective solution is the combined use of the mitigation technique discussed here together with the one presented in Sec. 4: a separation grid at $x_g \simeq 0.6L$, with $V_g = -(x_g/L)V_o$, can be naturally coupled to a field-cage correction at the same coordinate and voltage. The range of E_x and the value of δy_{max} would be reduced by factors approximately equal to 2 and 3, respectively, or larger, in the case of major space-charge effects.

8 Thermal convection effects.

The fluid dynamics of large liquid-argon TPCs are studied with numerical evaluations [26]. The pattern of the liquid flow is affected by thermal gradients induced by heat transfer at the cryostat walls, by heat dissipated in electronics contained in the liquid – if present, and by liquid recirculation. The latter is performed for purification purposes, and contributes to fluid flow both directly and as an additional source of temperature non-uniformity. The value of the velocity field is typically predicted in the range of fractions of mm/s to several cm/s. For comparison, the drift velocity of positive ions in typical liquid argon devices is in the range of 5–10 mm/s. Therefore the space-charge density distribution and the pattern of longitudinal and transverse distortions may be altered in a significant way by fluid motion.

Large effects may be expected in the proximity of elements that constrain the pattern of fluid motion, like side walls and possibly the electrode structures. Asymmetries and anomalous behaviour of transverse distortions δy , δz near the field cages have been reported [7, 27], suggesting the relevance of convective motion, while others [8] have observed that at some distance from the field cage, the observed longitudinal effects $\delta x(x)$ are described in good approximation with the approach described in sections 2 and 6 without need to refer to fluid motion.

It is not clear yet how accurate can be a fluid dynamics model in predicting the distribution of space charge and the effects on drifting electrons, but studies are underway. Another desirable development would be a design of fluid recirculation, *i.e.* the geometry of inlets/outlets and the recirculation rate, that would take into account its influence on the distribution of ions, and minimise the related uncertainty in the prediction of space-charge effects.

9 Conclusions

The subject of space charge in large-size liquid argon TPC detectors has been reviewed, considering the effects on the longitudinal (drift time) and the transverse coordinates, and the implication on the measurement of the specific energy loss dE/dX . The subject is relevant for the important role that this detector technology is taking in present and future neutrino experiments.

Analytical description and numerical examples have been presented, underlying the dependence of the effects on detector size and operating conditions, and determining the adimensional parameters that drive the behaviour of the detector response. The potential enhancement of space-charge effects in dual-phase detectors with feedback of positive ions has been illustrated. Border effects, and the case of detectors with comparable longitudinal and transverse size have been discussed.

Two design solutions that mitigate the effects of space charge have been presented. In the simplest implementation, they can reduce by at least a factor 2 the longitudinal and transverse distortions, respectively.

The combination of the two solutions is a straightforward extension of the study presented here.

Appendices

A Analytical expressions and approximations

In the one-dimensional, basic model in which the electric field is described by Eq. 5, the integral of $E_x(x)$ is given by:

$$V(x) \equiv - \int_0^x E_x(x') dx' = -\frac{x}{2} E_x(x) - \frac{L E_a^2}{2 \alpha E_o} \ln \left(\frac{E_x}{E_a} + \frac{\alpha x E_o}{L E_a} \right). \quad (\text{A.1})$$

The value of E_a is determined by $V(L) = E_o L$. Figure 1 (and Fig. 5, for the case without ion feedback) shows the result of a numerical computation of E_a/E_o as a function of α . The following relations hold to first order in α^2 :

$$\begin{aligned} E_a/E_o &\simeq 1 - \alpha^2/6 && \text{anode, better than 0.01 (0.05) for } \alpha < 1.2 \text{ (1.6)}, && (\text{A.2}) \\ E_c/E_o &\simeq 1 + \alpha^2/3 && \text{cathode, better than 0.01 (0.05) for } \alpha < 0.75 \text{ (1.12)}, \\ E_x(x)/E_o &\simeq 1 + (\alpha^2/2)(x^2/L^2 - 1/3) && \text{better than 0.04 (0.14) for } \alpha < 1 \text{ (1.5) in full range of } x, \\ -V(x)/(E_o x) &\simeq 1 - (\alpha^2/6)(1 - x^2/L^2) && \text{better than 0.0043 (0.033) for } \alpha < 1 \text{ (1.5) in full range of } x. \end{aligned}$$

All these approximations fail as α approaches 2. The maximum deviation between $V(x)$ and $-E_o x$ is

$$\delta V_{\max} = [V(x) - E_o x]_{\max} \simeq \frac{\alpha^2 E_o L}{16}, \quad (\text{A.3})$$

which occurs at x_{\max} between $L/\sqrt{3}$ and $L/2$ for increasing values of α .

Approximations at higher order in α^2 have been obtained numerically:

$$\begin{aligned} E_a/E_o &\simeq (1 - \alpha^2/6 - \alpha^4/180) && \text{better than 0.01 (0.05) for } \alpha < 1.57 \text{ (1.82)}, && (\text{A.4}) \\ &\simeq (1 - \alpha^2/6 - \alpha^4/180 - \alpha^{10}/8500) && \text{better than 0.01 (0.05) for } \alpha < 1.89 \text{ (1.97)}. \end{aligned}$$

$$\begin{aligned} E_c/E_o &\simeq (1 + \alpha^2/3 - \alpha^4/30) && \text{better than 0.01 (0.05) for } \alpha < 1.30 \text{ (1.60)}, && (\text{A.5}) \\ &\simeq (1 + \alpha^2/3 - \alpha^4/29 + \alpha^6/360) && \text{better than 0.01 (0.05) for } \alpha < 1.59 \text{ (2.00)}. \end{aligned}$$

At the field cage ($y = 0$) of a detector of large widths $W_y, W_z \gg L$, and for z far from the field cage, the transverse component of the electric field is approximated by the expression

$$|E_y(x, 0)| \simeq [1.17 + 25.7x/L + 55.1(x/L)^2 - 80.7(x/L)^3] \times (\alpha^2 E_o / 100), \quad (\text{A.6})$$

with an accuracy of some per cent of the maximum value of $|E_y(x, 0)|$.

The x dependence of the factor $\kappa(x)$ describing $\partial E_y / \partial y(x)$ at $y = W_y/2, z = W_z/2$ is given with an accuracy of a few per cent by the expressions:

$$\kappa(x) = 0.53 \alpha^2 \frac{E_o}{L} \frac{x}{L} \left[1 - \left(\frac{x}{L} \right)^2 \right] \quad \text{for } L = W_y \ll W_z \quad (\text{A.7})$$

$$\kappa(x) = 0.41 \alpha^2 \frac{E_o}{L} \frac{x}{L} \left[1 - \left(\frac{x}{L} \right)^2 \right] \quad \text{for } L = W_y = W_z. \quad (\text{A.8})$$

For $W_y \gg L, W_z \gg L, L \ll z \ll (W_z - L), x \simeq L/2$ and $y \ll W_y/2$, the y dependence of $E_y(L/2, y)$ is approximated with an accuracy of a few per cent by

$$E_y(y) \simeq E_y(0) \times \exp(-2.56y/L - 0.32y^2/L^2) \equiv E_y(0) \times f_{L/2}(y). \quad (\text{A.9})$$

As discussed in Section 6, as y increases towards $W_y/2$, the effect of the field cage at $y = W_y$ becomes more relevant, determining $E_y(x, W_y/2) = 0$. The combined effect of the two boundaries is well described by

$$E_y(x, y) \simeq E_y(x, 0) \times [f_x(y) - f_x(W_y - y)] \quad (0 \leq y \leq W_y). \quad (\text{A.10})$$

This equation is valid at the level of few per cent relative accuracy for $L = 6$ m, $0 \leq x \leq L$ and $W_y = 12$ m, and better than 10% for $W_y = 6$ m.

B Analytical approximation with finite electron lifetime in one dimension

In one dimension (*i.e.*, far from the side walls) the set of equation describing the electric field and the charge density distributions for electron, positive and negative ions, including a finite electron lifetime, is:

$$\begin{aligned} \frac{dE}{dx} &= \frac{\rho^+ + \rho^-}{\varepsilon} \\ \frac{d(\rho^e v^e)}{dx} &= -K - \frac{\rho^e}{\tau_e} \\ \frac{d(\rho^+ v^+)}{dx} &= K \\ \frac{d(\rho^- v^-)}{dx} &= \frac{\rho^e}{\tau_e} \end{aligned}$$

where ρ^- , ρ^e , v^- and v^e are negative, and ρ^e is negligible when compared to ρ^+ and ρ^- . The dependence of v^e on E prevents a direct integration. An approximate solution can be found under the assumptions

$$\frac{|\rho^e|}{\tau_e} \ll K, \quad |v^e(E)| \simeq v^e(E_0) \equiv v_0^e,$$

which brings to $\rho^e \simeq -K(L-x)/v_0^e$, a reasonable approximation of the numerical solution shown in Fig. 4. The equations for ρ^+ , ρ^- and E can then be integrated directly as

$$\begin{aligned} \rho^+(x) &\simeq \frac{Kx}{\mu^+ E(x)} \\ \rho^-(x) &\simeq -\frac{K(L-x)^2}{2\lambda_0^e \mu^- E(x)} \\ E(x) &\simeq E_0 \sqrt{\left(\frac{E_a}{E_0}\right)^2 + \alpha_+^2 \left(\frac{x}{L}\right)^2 - \alpha_-^2 \left(\frac{L}{\lambda_0^e}\right) \left(\frac{x}{L} - \frac{x^2}{L^2} + \frac{x^3}{3L^3}\right)} \end{aligned}$$

where $\lambda_0^e = v_0^e \tau_e$. In the comparison with the numerical evaluation illustrated in Fig. 4, with $\alpha_+ = \alpha_- = 1.15$ and $\lambda_0^e/L = 2.58$, the analytical approximation is found to be accurate to 1% in the values of $E(x)$ and $\rho^+(x)$, and in the range (10–15)% in $\rho^-(x)$. For $\lambda_0^e/L = 1.29$, the accuracy is better than 2% and (10–30)% respectively.

C Electric field with separation grid and optimal configuration at lowest order in α^2

As discussed in section 4, with a separation grid placed at x_g with voltage $V_g = -\delta_g V_0 = -(x_g/L)V_0$, the electric field for $x \leq x_g$ is still given by equation 5:

$$E_x(x) = E_0 \sqrt{(E_a/E_0)^2 + \alpha^2 (x/L)^2} \quad (x < x_g), \quad (\text{C.1})$$

with the only difference that the value of the electric field at the anode E_a is derived from the dependence of E_a vs. α , shown in Fig. 1 and in Eq.s A.2, A.4, after replacing α with $\delta_g \alpha$. Since at lowest order the

effects of space charge are proportional to α^2 , in the region between the anode and the grid the distortion to the electric field is reduced by a factor δ_g^2 . The value of δ_g cannot be too small, though, in order to preserve favourable effects of the grid on the side $x > x_g$.

In the region $x \geq x_g$, the boundary condition on the flux of positive ions is

$$(\rho^+ v_x^+)(x = x_{g+}) = (\rho^+ v_x^+)(x = x_{g-}) \times (E_{g+}/E_{g-}) = K x_g (E_{g+}/E_{g-}), \quad (\text{C.2})$$

where $K x_g$ is the ions flux reaching the grid from the $x < x_g$ side, which cross the grid at a fraction equal to the ratio of electric field on the two sides. The continuity equation provides

$$\rho^+(x) = \frac{K(x - x_g) + K x_g (E_{g+}/E_{g-})}{\mu^+ E_x(x)} \quad (x > x_g), \quad (\text{C.3})$$

and the corresponding differential equation for $E_x(x)$ is directly integrated as given in Eq. 20.

The optimal grid position x_g may be chosen so that in the corresponding case without grid, the field variation between $x = 0$ (anode) and $x = x_g$ is equal to half of the total variation across the gap, so that the range of variation in E_x in the two regions is approximately equal. At first order in α^2 , the position determined in this way is $x_g \simeq (1/\sqrt{2})(1 - \alpha/16)$. Next, the value of δ_g is chosen so that the range of E_x is equal in the two region, namely: $E_a = E_{g+}$, $E_{g-} = E_c$.

As an example, for $\alpha = 1.6$, the parameters of the optimal configuration are shown in first line of Table C.1, together with the corresponding values of E_x at the electrodes. The full range $(E_{x|\max} - E_{x|\min})/E_o$ is 0.503, to be compared to 1.161 without the grid. The closeness between the values $x_g/L = 0.642$ and $\delta_g = 0.626$ suggests to consider the configuration with equal values, which is shown in the third line of the table, and for which the range in E_x/E_o is increased by 0.052 only, and the lowest value of E_x/E_o is reduced by 0.034, which is also a small value, when compared to the difference of 0.270 obtained with the configuration without grid. Therefore the condition $x_g/L = \delta_g$ does not affect significantly the optimisation of the separation grid.

Additional examples that approach optimisation within the constrain $x_g/L = \delta_g$ are shown in other lines of Table C.1, together with a set of values obtained for $x_g/L = \delta_g = 0.7$, which are used in Fig. 7. For $\alpha = 2$, the ranges of E_x/E_o is 14% wider with x_g/L equal to 0.7 rather than 0.6, but the values $E_{x|\min}/E_o$ are similar, 0.63 and 0.65 respectively, so that in the end the effectiveness of the separation grid does not depend much on the choice of the value x_g/L within the range 0.6 to 0.7.

Table C.1: Examples of configurations of separation grid and resulting values of the electric field at the electrodes. The last three lines refer to the case shown in Fig. 7.

α	x_g/L	δ_g	E_a/E_o	E_{g-}/E_o	E_{g+}/E_o	E_c/E_o
1.6	0.642	0.626	0.792	1.295	0.792	1.295
0.8	0.68	0.68	0.953	1.097	0.925	1.075
1.6	0.64	0.64	0.822	1.313	0.758	1.260
2.0	0.60	0.60	0.748	1.414	0.630	1.376
0.8	0.7	0.7	0.950	1.103	0.925	1.067
1.6	0.7	0.7	0.783	1.366	0.790	1.215
2.0	0.7	0.7	0.650	1.544	0.716	1.285

D Parameters for field cage correction for reduction of the transverse components of the electric field

For a detector with wide aspect ratio $L \ll W_y, W_z$, and considering only positive ions, the voltage difference $\delta V_{fc}(x)$ between a point of drift coordinate x and transverse coordinates y, z far from the field cage

and the corresponding voltage at the position x of a linear field-cage is given by the voltage distortion $\delta V(x)$ in the one-dimensional description of the effects of space charge. Near the field cage, the voltage difference generates transverse components of the electric field according to Eq. 21, and the most effective position x_{fc} for a correction to the voltage profile of the field cage is at the maximum of $\delta V_{fc}(x)$.

For $\alpha < 1.5$, $\delta V_{fc}(x) = V(x) + E_o x$ is approximated using Eq.s A.2, and the preferred coordinate is $x_{fc} \simeq L/\sqrt{3}$. A correction voltage $V_{fc} = -(E_o L/\sqrt{3})(1 - \alpha^2/9)$ is applied to the field cage at that point in order to cancel δV_{fc} locally and reduce it in the full range $0 < x < L$. Compared to a field cage without correction, the current flowing from the anode to x_{fc} is reduced by a fraction equal to $\alpha^2/9$, the current flowing from x_{fc} to the cathode is increased by a fraction equal to $\alpha^2/[9(\sqrt{3} - 1)]$, with the difference of about $0.26\alpha^2$ being provided at the intermediate connection.

Once the correction is applied, $\delta V_{fc}(x)$ takes a different shape and two local maxima occur at $x = (1/3)L$ and $x \simeq 0.80L$. The values of the maxima are equal to $\alpha^2 E_o L/81$ and about $\alpha^2 E_o L/57$ respectively, much smaller than $\alpha^2 E_o L/16$ obtained without correction to the field cage.

For larger values of α , without applying the correction, the maximum of $\delta V_{fc}(x)$ moves towards $x = L/2$. For instance, for $\alpha = 1.5$, the preferred value is $x_{fc} \simeq 0.54L$, with the maximum of $\delta V_{fc}(x)$ still approximated by $\alpha^2 E_o L/16$ within about 1%.

When negative ions from electron capture are present, smaller values of $\delta V_{fc}(x)$ are found for the same value of α . Computation performed with $\tau_e = 10$ ms, $L = 6$ m, $E_o = 500$ V/cm and $\alpha = 1.15$, have shown that, without the correction, $\delta V_{fc}(x)$ is about 10% smaller than in the case with infinite electron lifetime, with the coordinate at the maximum of δV_{fc} still well approximated by $x \simeq L/\sqrt{3}$.

References

- [1] S. Palestini et al., *Space charge in ionization detectors and the NA48 electromagnetic calorimeter*, Nucl. Instrum. Methods Phys. Res. A **421** (1999) 7.
- [2] B. Toggerson et al., *Onset of space charge effects in liquid argon ionization chambers*, Nucl. Instrum. Methods Phys. Res. A **608** (2009) 238–245.
- [3] J.P. Rutherford and R.B Walker, *Space-charge effects in liquid argon ionization chambers*, Nucl. Instrum. Methods Phys. Res. A **776** (2015) 65-74.
- [4] C.D. Child, *Discharge from hot CaO*, Phys. Rev. (Series I) **32**, 492 (1911).
- [5] I. Langmuir, *The effect of space charge and residual gases on thermionic currents in high vacuum*, Phys. Rev. 2, **450** (1913); *The pure electron discharge and its applications in radio telegraphy and telephony*, Proc. Inst. Radio Eng. **3**, 261 (1915).
- [6] J.N. Marx and D.N. Nygren, *The time projection chamber*, Physics Today **31**,10, 46 (1978); Aihara et al., *Spatial resolution of the PEP-4 time projection chamber*, IEEE Trans. Nucl. Sci. **30**, 1,(1983) 76.
- [7] M. Mooney, *The MicroBooNE experiment and the impact of space charge effects*, Proc. APS/DPF 2015 Meeting, M. Tecchio and D. Levin (Eds.), arXiv: 1511.01563 [physics.ins-det]; MicroBooNE Collaboration, *Study of space charge effects in MicroBooNE*, MICROBOONE-NOTE-1018-PUB.
- [8] ICARUS Collaboration, M. Antonello et al., *Study of space charge in the ICARUS T600 detector*, JINST **15**, July 2020, arXiv:2001.08934 [physics.ins-det]
- [9] DUNE Collaboration, B. Abi et al., *The single-phase ProtoDUNE technical design report*; arXiv:1706.07081v2 [physics.ins-det].
- [10] L. Agostino et al., *LBNO-DEMO: Large-scale neutrino detector demonstrators for phased performance assessment in view of a long-baseline oscillation experiment*, CERN-SPSC-2014-013 (SPSC-TDR-004), arXiv:1409.4405v1 [physics.ins-det].

- [11] B.L. Henson, *Mobility of positive ions in liquefied argon and nitrogen*, Phys. Rev. **135**, A1002
- [12] T.H. Dey and T.J. Lewis, *Ion mobility and liquid motion in liquefied argon*, J. Phys. D: Applied Physics **1** (1968) 1019–1029
- [13] ATLAS Collaboration, *ATLAS liquid argon calorimetry: TDR*, CERN-LHCC-96-041.
- [14] C. Rubbia, *The liquid-argon time projection chamber: a new concept for neutrino detectors*, CERN-EP/77-08 (1977).
- [15] W. Walkowiak, *Drift velocity of free electrons in liquid argon*, Nucl. Instrum. Methods Phys. Res. A **449**, 288 (2000).
- [16] ICARUS Collaboration, S. Amoruso et al., *Study of electron recombination in liquid argon with the ICARUS TPC*, Nucl. Instrum. Methods Phys. Res. A **523** (2004) 275-286.
- [17] G. Bakale, U. Sowada and W.F. Schmidt, *Effect of an electric field on electron attachment to sulfur hexafluoride, nitrous oxide, and molecular oxygen in liquid argon and xenon*, J. Phys. Chem. **80** (1976) 2556–2559;
A. Bettini et. al., *A study of the factors affecting the electron lifetime in ultrapure liquid argon*, Nucl. Instrum. and Methods Phys. Res. A **305** (1991) 177–186.
- [18] COMSOL Multiphysics[®], COMSOL AB, Stockholm, Sweden.
- [19] A. Bueno et al., *Nucleon decay searches with large liquid argon TPC detectors at shallow depths: atmospheric neutrinos and cosmogenic backgrounds*, JHEP **04** (2007) 41, arXiv:hep-ph/0701101.
- [20] B. Aimard et al, *A 4 tonne demonstrator for large-scale dual-phase liquid argon time projection chambers*, JINST **13**, November 2018, arXiv:1806.03317v3 [physics.ins-det].
- [21] C. Cantini et al., *Performance study of the effective gain of the double phase liquid Argon LEM Time Projection Chamber*, JINST **10**, March 2015, arXiv:1412.4402 [physics.ins-det].
- [22] See for instance J.D. Jackson, *Classical Electrodynamics*, Wiley, New York-London, 1962, p. 111–113.
- [23] W. Tauchert, H. Jungblut and W.F. Schmidt, *Photoelectric determination of V_0 values and electron ranges in some cryogenic liquids*, Can. J. Chem. **55**, 1860 (1977).
- [24] L. Romero, R. Santorelli and B. Montes, *Dynamics of the ions in Liquid Argon Detectors and electron signal quenching*, Astropart. Phys. **92** (2017) 11-20, arXiv:1609.08984 [physics.ins-det].
- [25] L. Bruschi et al, *Transmission of negative ions through the liquid-vapour surface in neon*, J. Phys. C: Solid State Phys. **8** (1975) 1412.
- [26] For instance, E. Voirin. *Turbulent diffusion and its effects on the ion distribution field of the Micro-BooNE LAr Cryostat*, MicroBooNE Technical Note 1895.
- [27] DUNE Collaboration, B. Abi et al., *First results on ProtoDUNE-SP liquid argon time projection chamber performance from a beam test at the CERN Neutrino Platform*, arXiv:2007.06722 [physics.ins-det].